THE JOURNAL OF PHYSICAL CHEMISTRY B
A JOURNAL OF THE AMERICAN CHEMICAL SOCIETY

pubs.acs.org/JPCB

Article

Mechanistic Insights into the Selectivity for Arsenic over Phosphate Adsorption by Fe^{3+}-Cross-Linked Chitosan Using DFT

Obinna Nwokonkwo and Christopher Muhich*

Cite This: *J. Phys. Chem. B* 2024, 128, 1689−1699

Read Online

ACCESS | Metrics & More | Article Recommendations | Supporting Information

ABSTRACT: Fe^{3+}-cross-linked chitosan exhibits the potential for selectively adsorbing arsenic (As) over competing species, such as phosphate, for water remediation. However, the effective binding mechanisms, bond nature, and controlling factor(s) of the selectivity are poorly understood. This study employs ab initio calculations to examine the competitive binding of As(V), P(V), and As(III) to neat chitosan and Fe^{3+}-chitosan. Neat chitosan fails to selectively bind As oxyanions, as all three oxyanions bind similarly via weak hydrogen bonds with preferences of P(V) = As(V) > As(III). Conversely, Fe^{3+}-chitosan selectively binds As(V) over As(III) and P(V) with binding energies of −1.9, −1, and −1.8 eV for As(V), As(III), and P(V), respectively. The preferences are due to varying Fe^{3+}−oxyanion donor−acceptor characteristics, forming covalent bonds with distinct strengths (Fe−O bond ICOHP values: − 4.9 eV/bond for As(V), − 4.7 eV/bond for P(V), and −3.5 eV/bond for As(III)). Differences in pK_a between As(V)/P(V) and As(III) preclude any preference for As(III) under typical environmental pH conditions. Furthermore, our calculations suggest that the binding selectivity of Fe^{3+}-chitosan exhibits a pH dependence. These findings enhance our understanding of the Fe^{3+}−oxyanion interaction crucial for preferential oxyanion binding using Fe^{3+}-chitosan and provide a lens for further exploration into alternative transition-metal−chitosan combinations and coordination chemistries for applications in selective separations.

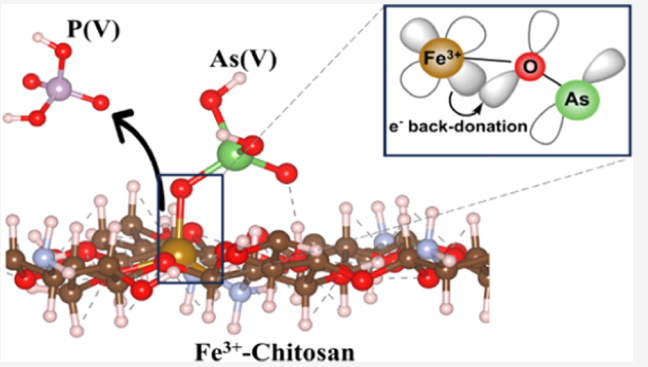

1. INTRODUCTION

The efficient removal of arsenic (As) from competitive water matrices remains a pressing challenge, especially in distributed drinking water systems. As is highly toxic, nonbiodegradable, and mobile even at low concentrations.[1] Excessive ingestion of As can cause ulcers, skin cancer, liver, kidney, and lung deterioration,[1,2] and potentially longer-term neurodegenerative disorders. Therefore, the World Health Organization (WHO) recommends a maximum concentration of 10 μg of As/L in drinking water.[3] As is a metalloid typically present in water as pentavalent As(V) (arsenate) or trivalent As (III) (arsenite) oxyanions, where their specific protonation state and ionic charge are controlled by the pH (the environmentally relevant pK_a's are 6.9 and 9.2 for As(V) and As(III), respectively).[4−8]

As removal technologies include oxidative processes, precipitation, ion exchange, membrane processes (reverse osmosis, nanofiltration, electrodialysis), and adsorption.[4,9−16] Adsorption is an attractive, inexpensive technology with great promise for under-the-sink water remediation applications, particularly in decentralized drinking water systems. Unlike some state-of-the-art technologies available for municipal scale use, adsorption requires no chemical input, is reasonably fouling-resistant, and can attain high removal efficiencies.[16−19] However, in most contaminated waters, the performance and longevity of conventional adsorbents are stymied by the presence of other, often less toxic, species such as phosphate, silicate, sulfate, nitrate, and bicarbonate.[16,20,21] These competing species are usually chemically and structurally similar to As oxyanions (As(III) and As(V)) and may occur at significantly higher concentrations (up to 10−100 times);[22] thus, they compete with As oxyanions for nonspecific sites of unselective sorbent materials resulting in decreased treated water volumes before As breakthrough.[4,23,24] Selective sorbent materials could enhance As removal efficiencies and capacity,[25] thus lowering treatment costs by decreasing sorbent replacement frequency.

Chitosan (CS) is a biopolymer with appealing properties for a sustainable sorbent, namely, its biodegradability, versatility, biocompatibility, and metal−oxyanion binding capabilities.[26,27] The adsorptive capability of CS is primarily due to the abundance of functional groups, including amine and hydroxyl groups, in its molecular structure, which serves as binding sites for target pollutants in water.[28] For example, previous studies

Received: October 14, 2023
Revised: January 23, 2024
Accepted: January 26, 2024
Published: February 14, 2024

https://doi.org/10.1021/acs.jpcb.3c06838
J. Phys. Chem. B 2024, 128, 1689−1699

revealed that CS binds anionic compounds, such as As(V), at protonated amine sites via electrostatic attraction.[29,30] However, despite binding oxyanions, CS is nonselective in complex water matrices, i.e., those containing a mixture of pollutants, inhibiting its toxin removal capacity.[30]

Recent attention has focused on inducing selectivity in CS sorbents. For example, Yamani et al. revealed that including Cu^{2+} as a cross-linking agent in CS enables selective As(V) adsorption over phosphate (P(V))[31,32] despite the well-known similarity in the oxyanion structure, chemical nature, and binding behaviors.[33−38] They attributed the selectivity to mild differences in molecular size, partial charge densities, and polarizabilities between the oxyanions, which cause more favorable electrostatic interactions between Cu^{2+}-chitosan and As(V) than phosphate P(V).[31,32] However, Cu^{2+}-chitosan only selectively binds the more challenging As(III) after pre-photooxidation, which increases the complexity of point-of-use remediation systems.[25,32] Pincus et al. examined other cross-linker ions and reported that while Fe^{3+}, Ni^{2+}, and Zn^{2+}-chitosan systems outperformed Cu^{2+} and Al^{3+} in terms of the quantity of As removed, only Fe^{3+} achieved selectivity for both As species over P(V) due to differences in inner-complexation behaviors.[39]

Density functional theory (DFT) has been applied to predict the molecular and electronic structures of chitosan oligomers of various lengths.[40,41] Rahangdale et al. studied the binding of organic molecules by molecularly imprinted chitosan.[42] The binding of heavy-metal cations to neat chitosan has also been examined.[43−49] Although there have been several computational studies of metal cation binding to chitosan, there has been much less attention to heavy-metal−oxyanion binding to neat and modified chitosan. Mishima et al. studied chromate binding on epichlorohydrin and glutaraldehyde cross-linked chitosan.[50] Despite their experimental promise, transition-metal cross-linked chitosan (TMC) has not been extensively examined with computational models for their ability to bind toxic oxyanions selectively. To our knowledge, only Pincus et al. have attempted to examine these systems using DFT. In their study, they used DFT to predict the geometric structure of As(III), As(V), and P(V) binding to Cu^{2+}, Ni^{2+}, and Fe^{3+} as a reference point to explain extended X-ray absorption fine structure (EXAFS) results. While this study successfully showed that the oxyanions bind in an inner-sphere configuration to TMCs in agreement with the experimental results, the relative energetics, binding preferences, underlying electronic behavior, and pH effects were not reported or explicitly considered.[39] These properties are crucially important due to the sensitivity of binding to pH effects and considering the use of pH swings for adsorption/desorption cycles.[51] A better understanding of the underlying mechanism that leads to differences between As and P binding could enable directed design of these materials to improve selectivity by increasing the desirable electronic and geometric structures.

Therefore, in this study, we closely examine the competitive binding of As(V), As(III), and P(V) to Fe^{3+}-chitosan using DFT calculations to identify the underlying causes of their relative selectivity. The findings of this work elucidate the role of the transition-metal ion in strong and selective oxyanion binding and provide new knowledge that can be applied to separate similar oxyanion species based on mild differences in oxyanion ligand characters.

2. COMPUTATIONAL DETAILS

2.1. First-Principles Calculations. DFT calculations were performed using the Vienna Ab initio Simulation Package (VASP),[52,53] with periodic boundary conditions. Calculations were completed with the HSE06 hybrid meta-generalized gradient approximation (GGA) functional[54] because the pure GGA Perdew−Burke−Ernzerhof (PBE) functional[55] overestimated the binding energies of the species by up to 0.4 eV compared to HSE06 (see Figure S1). The Projector Augmented Wave (PAW) pseudopotential approximation[56] lowered computational costs by only explicitly including valence electrons. PAWs explicitly calculated transition metal's 4s and 3d orbitals, while nonmetals (C, N, and O) describe the 2s and 2p orbitals, and H, the 1s orbital. A summation of plane waves with kinetic energies up to 600 eV composed the wave functions. Including higher energy waves (700 eV) resulted in only a 0.05 and 0.03 eV improvement in total binding energies and binding energy differences, respectively. The Brillouin zone was sampled at the Γ-point for all calculations because there was no significant changein calculated binding energies with higher *k*-point meshes, e.g., going from a 1 × 1 × 1 to a 2 × 1 × 1 *k*-mesh for the cross-linked polymer model resulted in only a 0.01 eV decrease in binding energy. All calculations were spin-polarized, and van der Waals dispersion forces were accounted for via the empirical DFT-D3 method of Grimme et al.[57,58] Implicit water solvation was implemented in the system via the polarizable continuum model (PCM)[59] (implemented in VASP) to account for solvating effects on the binding of species.[59−61]

CS was modeled as a periodic chain of tetramers (∼21.15 Å) linked to its periodic images via a *β*-oxygen linkage as shown in Figure S2. Fe^{3+} cross-linking of the Fe^{3+}-chitosan (Fe^{3+}-CS) system occurred between proximal amine and hydroxyl groups of a CS tetramer and a dimer. We used a tetramer chitosan model for our study because increasing the model beyond this size did not significantly alter the local metal−oxyanion interactions of interest at the metal site either chemically or sterically. Increasing from the tetramer model to a hexamer model resulted in only a 0.05 eV difference in the predicted selectivity between As(V) and P(V). Hence, the tetramer model was used for all of the calculations in this study. Two orientations of chitosan chains relative to each other were sampled for the system: parallel (Θ = 180°) and perpendicular (Θ = 90°). The configurations are shown in Figure 1a,b, while the oxyanions are shown in Figure 1c. These orientations were chosen because they are the extreme cases for the cross-link between the chitosan oligomers at the minimum energy amine sites of chitosan. We note that there exists a continuum of possible rotation angles and configurations at the cross-link site, which is prohibitively computationally expensive to sample using DFT methods. Therefore, we selected the extreme cases for analysis. A more detailed sampling of the TMC mesoscale structure for other possible cross-link configurations using molecular mechanics of larger system sizes is being conducted as part of follow-up work. In the parallel orientation, the axis of the CS dimer is ∼180° rotated from the axis of the tetramer chain, and the cross-link site consists of a square planar coordination complex between Fe^{3+} and the CS molecules' neighboring N and O atoms. In the perpendicular configuration, the CS dimer is rotated by 90° along the cell *y*-axis, resulting in a smaller N−Fe−N bond angle at the cross-link site. The parallel orientation was lower

https://doi.org/10.1021/acs.jpcb.3c06838
J. Phys. Chem. B 2024, 128, 1689−1699

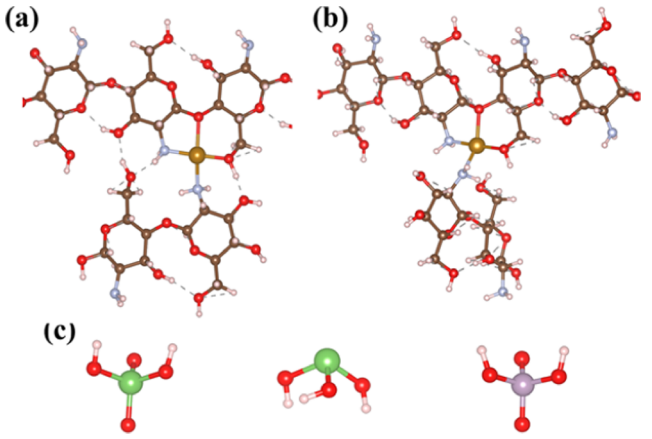

Figure 1. Molecular models of Fe^{3+}-CS in the (a) parallel and (b) perpendicular configurations and (c) molecular models for As(V), As(III), and P(V). H, O, N, C, P, Fe, and As are represented by white, red, light blue, dark brown, purple, light brown, and green spheres, respectively.

in energy than the perpendicular one by −0.1 eV and was used for all subsequent binding calculations. A vacuum space > 15 Å was applied in the direction normal to the cross-linking plane for all systems to avoid interactions across the periodic images of the simulation cells in that direction, while the length of the CS chain ensures similar separation in the other directions. Molecular structures were relaxed until atomic forces were less than 0.001 eV/Å.

Oxyanion binding on neat CS was studied at an amine binding site due to more favorable binding interactions than at a hydroxyl site. As(V) and P(V) bind more favorably at the amine site than at a hydroxyl site by 0.1 eV. These results are consistent with previous experimental findings.[30,62] Different configurations for oxyanion binding involving Fe^{3+} and nearby hydroxyl sites were considered for the Fe^{3+}-CS system; we report on only the lowest energy configuration for each oxyanion. Binding energies for all systems were calculated using eq 1.

$$\Delta E_{\text{bind}} = E_{\text{CS/Fe}^{3+}\times\text{oxo}} - E_{\text{CS/Fe}^{3+}+\text{oxo}} \tag{1}$$

where ΔE_{bind} is the binding energy for oxyanion, $E_{\text{CS/Fe}^{3+}+\text{oxo}}$ is the total energy of the system with oxyanion (As(V), As(III), or P(V)) removed from CS/Fe^{3+} in the same simulation box, and $E_{\text{CS/Fe}^{3+}\times\text{oxo}}$ is the system's total energy with the oxyanion bound at a CS site or Fe^{3+} for Fe^{3+}-CS. This procedure was necessary to achieve charge consistency across all simulation cells and eliminate the potential discrepancies that may arise from using a background Jellium charge. A negative value for the binding energy represents an exothermic process, while a positive value corresponds to an endothermic process.

2.2. Chemical Bonding Analysis. Crystal Orbital Hamilton Population (COHP) analysis was performed using the Lobster v3.1[63] and Pymatgen packages.[64,65] COHP weights orbital energies from the Density of States (DOS) by the corresponding elements of the Hamiltonian and thus partitions the band-structure energy into bonding, nonbonding, and antibonding contributions. Thus, the Integrated Crystal Orbital Hamilton Population (ICOHP) up to the Fermi level quantifies the strength of the chemical bonds between atomic species. Because the ICOHP value indicates the energy associated with the interaction between atoms and orbitals, we use it to characterize the relative extents of metal−ligand back-donation as a measure of the π-acceptor character of oxyanions in our transition-metal system.

2.3. As(V) Removal Prediction. Using relevant equilibrium relationships, we predicted the percentage removal of As(V) on Fe^{3+}-CS as a function of pH. The Gibbs free energies of binding were calculated as follows

$$\Delta G_{\text{bind}} = \Delta E_{\text{bind}} - T\Delta S - 2.3RT(\text{pH} - \text{p}K_{\text{a}}) \tag{2}$$

where ΔE_{bind} is the electronic binding energy calculated from eq 1 for various As(V) and P(V) molecules. R is the gas constant, T is the temperature, taken to be 298 K, and the third term accounts for the pH-dependent free energy for deprotonated oxyanions. We assumed that an oxyanion loses half of its aqueous phase entropy upon binding; hence, ΔS was taken as half the negative of the free ion entropy in solution S_{aq} (from refs 66,67). We performed a sensitivity analysis to ascertain the consequence of assuming half solution-entropy loss on selective removal of As(V) and P(V) by Fe^{3+}-CS. As shown in Figure S9, we find that the selective oxyanion removal is only slightly influenced by the amount of solution phase entropy retained upon binding, except for the extreme and unrealistic case of no entropy loss. A lower onset pH for selective As(V) removal is predicted when more entropy is retained upon binding: 52% As(V) removal at pH 6.8, 58% at pH < 6, and 87% at pH < 6 for 100, 50%, and no entropy loss, respectively. Moreover, we obtain the closest match with the experimentally measured competitive As(V) removal[39] amounts assuming a 50% entropy loss. We note that while this estimation shifts the quantitative results slightly, it does not alter the overall characteristics of our findings. We only computed ΔG_{bind} for the diprotonated and monoprotonated As(V) and P(V) species ($H_2XO_4^-$ and HXO_4^{2-}) since those are present in environmental conditions. Equilibrium binding constants were calculated using

$$K = \exp\left(\frac{-\Delta G_{\text{bind}}}{RT}\right) \tag{3}$$

where K is the equilibrium constant for a given oxyanion species. Equilibrium concentrations of the two oxyanion protonation states were calculated using the pK_{a} values for As(V) and P(V) (6.9 and 7.2, respectively) and the relationship

$$\text{p}K_{\text{a}} = \text{pH} + \log\left(\frac{[H_2XO_4^-]}{[HXO_4^{2-}]}\right) \tag{4}$$

To examine the competition between the As(V) and P(V) species, the fractional occupation of the binding sites for a given As(V) species with the number of protons y was estimated using eq 5 as in ref 68

$$\theta_{\text{As},y} = \frac{K_{\text{As}}[H_yAsO_4^{y-3}]}{1 + K_{\text{As},y}[H_yAsO_4^{y-3}] + K_{\text{P},y}[H_yPO_4^{y-3}]} \tag{5}$$

3. RESULTS AND DISCUSSION

To understand the differences in adsorptive selectivity of CS and Fe^{3+}-CS, we used DFT to calculate the binding energies of As(V), As(III), and P(V), the closest structural analogue competitor to As(V). We first discuss the binding to CS and Fe^{3+}-CS of the semiprotonated states of As(V) and P(V) ($H_2AsO_4^-$ and $H_2PO_4^-$) and the fully protonated state of As(III) (H_3AsO_3) because these are the most present species

https://doi.org/10.1021/acs.jpcb.3c06838
J. Phys. Chem. B 2024, 128, 1689−1699

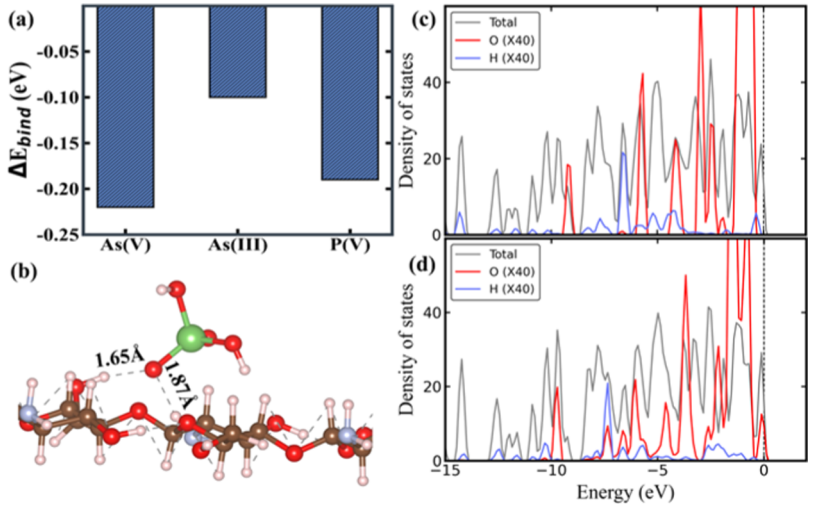

Figure 2. (a) Oxyanion binding energies on neat CS, (b) optimized structure for CS-As(V), and DOS plots for (c) before and (d) after As(V) binding to neat CS. H, O, N, C, and As are represented by white, red, light blue, dark brown, and green spheres, respectively.

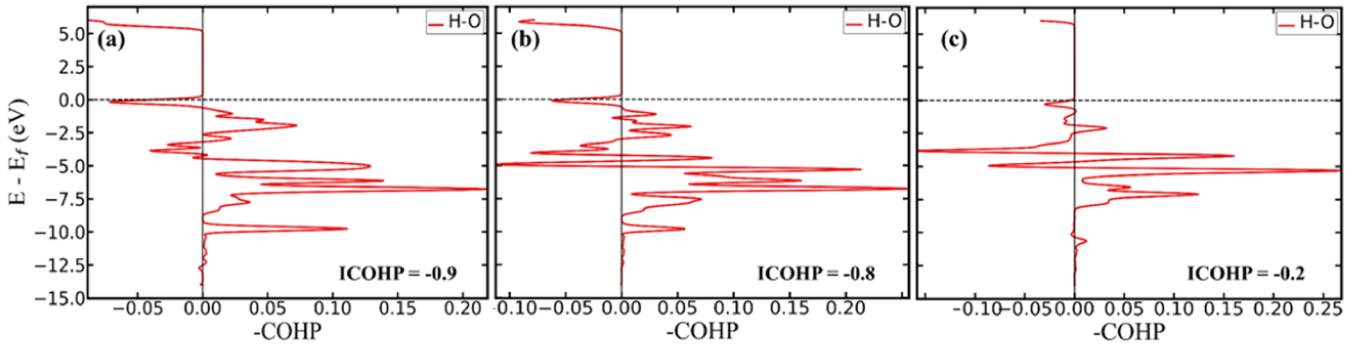

Figure 3. COHP plots for the H···O H-bond for (a) As(V), (b) P(V), and (c) As(III) bound to neat CS. Insets: ICOHP values that characterize bond strengths.

at neutral pH (~7). Subsequently, we report on the effects of oxyanion protonation on binding.

3.1. As(V) Binding to Neat Chitosan. We calculate that neat CS binds As(V) exothermically by −0.2 eV, as shown in Figure 2a. The optimized binding configuration, shown in Figure 2b, reveals that As(V) binds in a bidentate configuration via weak H-bonding to a CS amine site and a neighboring OH site. When As(V) is unbound and far from the binding site, there is minimal overlap between the electronic states of the As(V) O atom and the CS H atom (Figure 2c). The As(V) O atom states populate the higher energy regions of the system near the Fermi level, while the H atom states populate lower energy regions. Subsequently, when As(V) is within proximity of the binding site, there is a slight redistribution and overlap of electronic states between the As(V) O atom and CS H atoms, indicative of weak interaction, shown in Figure 2d. The weak interaction results in a mean H···O bond distance of 1.76 Å, which is slightly longer than the typical H···O hydrogen bond (~1.7 Å[69]) and nearly double O−H covalent bond length (~0.98 Å), indicating that neat CS binds As(V) via weak H-bonding. There is no significant charge transfer between As(V) and CS (only $-0.08e^-$) and we calculate an ICOHP value of −0.9 eV/bond for the H···O bond, consistent with the negligible overlap of states and weak binding energy. Overall, we predict that neat CS is a poor binding agent for As(V), as is seen experimentally,[24] due to the absence of significant chemical bonding, which relegates CS-As(V) interactions to weak H-bonds.

CS binds P(V) in a manner nearly identical to that of As(V) with a binding energy of −0.2 eV (Figure 2a). P(V) also binds in a bidentate configuration with neighboring amine and hydroxyl sites with a mean CS−P(V) bond distance (1.81 Å) only 0.05 Å longer than that of As(V), in agreement with the equal binding energies for both oxyanions, as shown in Figure S3. In addition to the CS−P(V) bond distance, which shows that CS also binds P(V) via H-bonding, the PDOS reveals a similar electronic structure for the CS−P(V) interaction like As(V), indicative of its weak covalent character (see Figure S3). We also calculate nearly equal charge transfer, $-0.14e^-$, and mean ICOHP value, −0.8 eV/bond, respectively, for P(V) and As(V), in agreement with the similar binding energies, confirming that both oxyanions bind with equal strength and mechanism to CS. Figure 3 shows the COHP plots for binding both oxyanions to neat CS. We attribute the similarity in binding behaviors between P(V) and As(V) to their nearly identical structure and charge on O atoms, which equates to highly similar electrostatic interactions with CS. Our results agree with the experimental work by Yamani and co-workers,[31] who showed low removal efficiencies for As(V) with background P(V) using neat chitosan.

CS binding of As(III) is weaker than the other oxyanions with a binding energy of only −0.1 eV. The weak As(III) binding is characterized by a longer H···O bond distance of

https://doi.org/10.1021/acs.jpcb.3c06838
J. Phys. Chem. B 2024, 128, 1689−1699

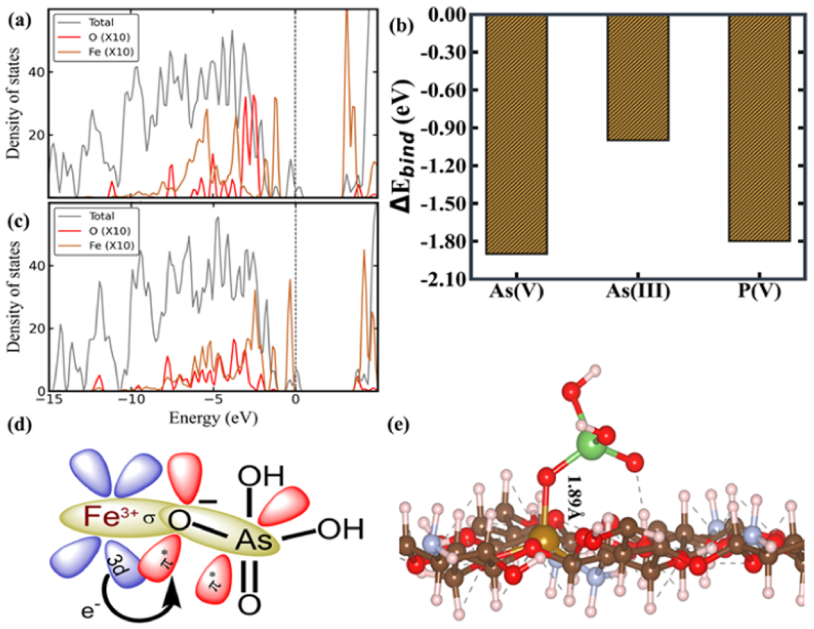

Figure 4. (a) DOS plot before As(V) binding to Fe^{3+}-CS, (b) oxyanion binding energies on Fe^{3+}-CS, (c) DOS plot for As(V) bound to Fe^{3+}-CS, and (d) schematic diagram of the orbital interactions involved in the Fe−O bond between Fe^{3+}-CS and As(V). The diagram illustrates the back-donation of electron density from Fe 3d orbitals to As(V) π^* antibonding orbitals. (e) Optimized structure for As(V) bound to Fe^{3+}-CS. H, O, N, C, Fe, and As are represented by white, red, light blue, dark brown, light brown, and green spheres, respectively.

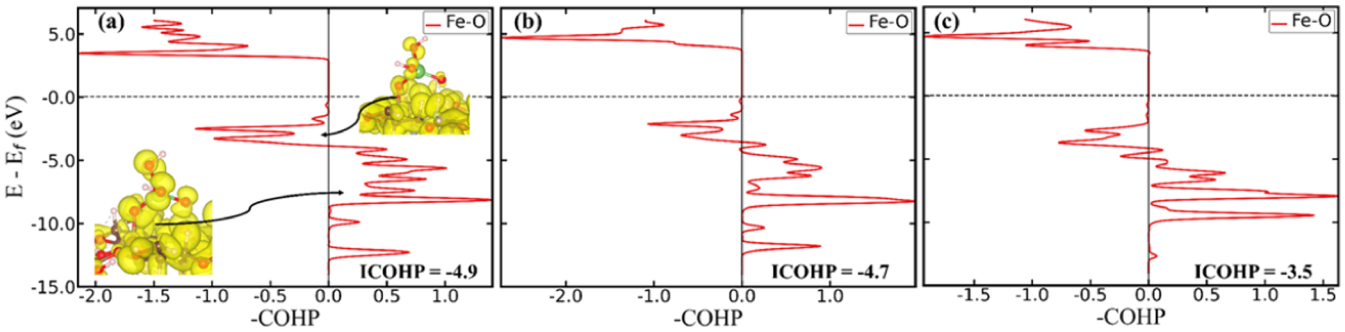

Figure 5. COHP plots for the Fe−O bond for (a) As(V), (b) P(V), and (c) As(III) bound to Fe^{3+}-CS. Insets are ICOHP values that characterize bond strengths and partial charge plots for the highlighted filled bonding and antibonding regions for As(V).

2.19 Å compared to the shorter bonds for As(V) and P(V), 1.76 and 1.81 Å, respectively. Further, the lack of charge transfer and less negative ICOHP value (−0.2 eV/bond) indicate that no chemical bond was formed. CS binds As(III) less preferentially than As(V) and P(V) because of its weaker electrostatic attraction to the charge-neutral As(III) (H_3AsO_3) compared to the negatively charged As(V) and P(V) ($H_2AsO_4^-$ and $H_2PO_4^-$). Overall, we predict relative binding preferences of P(V) = As(V) > As(III) with neat chitosan.

3.2. As(V) Binding to Fe^{3+}-Chitosan. We investigated As and P(V) binding to Fe^{3+}-CS. The cross-linking of CS with Fe^{3+} introduces high-energy Fe 3d-states into the Fe^{3+}-CS electronic structure near the Fermi level, shown in Figure 4a. The geometry of the chain is unchanged, with only a minor reorganization of two internal H-bonds of the CS tetramer in the vicinity of the cross-link. Additionally, two new H-bonds were formed between the tetramer and the dimer.

As(V) binds to Fe^{3+}-CS in a profoundly different manner than in the neat CS case. As(V) binds in a bidentate configuration to the Fe^{3+} center and an OH group and does so nearly 10 times more strongly (−1.9 eV) than neat CS (see Figure 4b). The increased binding strength is due to increased Coulombic attraction between the negatively charged As(V) and the positively charged Fe^{3+} and to additional chemical bonding. Two bonds form: a covalent bond between an O atom of As(V) and Fe^{3+} and an H-bond between As(V) and a nearby OH group on CS. A similar mixture of inner-sphere metal−oxyanion and CS-oxyanion H-bonds has been predicted for As(V) binding to Fe^{3+}-CS.[39,70] Further, we note that the inner-sphere complex is via a covalent bond, unlike previously reported.[39] The covalent bond forms due to the availability of similarly high-energy electronic states from As(V) and Fe^{3+} near the Fermi level. Before binding, both the O states from As(V) and Fe states form the near-Fermi region, as shown in Figure 4a. These electronic states redistribute upon As(V) binding (Figure 4c), allowing mixing and the formation of a set of bonding and antibonding molecular orbitals. The electron density donated by the O atom forms the σ-bond with the Fe.

Meanwhile, Fe^{3+} back-donates electron density, partially filling the As−O π^* antibond and forming additional bonding and antibonding states. The back-donation of electrons also lengthens the As−O bond of the O bound to Fe^{3+} by 0.05 Å,

https://doi.org/10.1021/acs.jpcb.3c06838
J. Phys. Chem. B 2024, 128, 1689−1699

Table 1. Bond Lengths and Binding Energies for As(V), As(III), and P(V) Bound to Fe^{3+}-CS

oxyanion	PH	species	AE_{bind} (eV)	As/P−Fe distance (Å)	As/P−O bond length (Å)	Fe−O bond length (Å)	refs
As(V)	–	$H_2AsO_4^-$	−1.9	3.23	1.72	1.89	this work
	6	$H_2AsO_4^-$	-	3.29	1.70−1.71	1.95	39
As(III)	-	H_3AsO_3	−1	3.44	1.92	2	this work
	6	H_3AsO_3	-	2.91	1.79−1.8	1.61	39
P(V)	–	$H_2PO_4^-$	−1.8	3.14	1.55	1.89	this work

consistent with the partial filling of their antibonding orbitals.[71] The interaction between the O 2p and Fe 3d electrons yields a strong coordinated Fe−O bond between As(V) and Fe^{3+} (ICOHP = −4.9 eV/bond) accompanied by lowered overall electronic energies that stabilize these states.[72,73] The ICOHP value for the 3d-π^* orbital interaction from back-donation is −0.8 eV/bond. The orbital interactions in the Fe−O bond are schematically shown in Figure 4d. COHP analysis corroborates the filling of these π^* antibonding states in agreement with the partial charge plots for the participant bands near the Fermi level, as shown in Figure 5a. The strong interaction causes the Fe−O bond length to be 1.89 Å, as shown in Figure 4e. This Fe−O bond length is only 0.06 Å shorter than the length deduced from the second shell fit of the Fe^{3+}-As(V) complex (1.95 Å) obtained via EXAFS analysis.[39] In addition, there is excellent agreement between our DFT calculations and EXAFS for the As−O bond of As(V) when bound to Fe^{3+}-CS, 1.72 and 1.70−1.71 Å,[39] respectively. Relevant bond lengths in the Fe^{3+}-As(V) complex are summarized in Table 1.

3.3. As(III) and P(V) Binding to Fe^{3+}-Chitosan. P(V) also binds nine times more favorably to Fe^{3+}-CS, −1.8 eV, than neat CS. Like As(V), P(V) binds to Fe^{3+} in a bidentate configuration via an Fe−O covalent bond and an H-bond. The Fe−O bond length between P(V) and Fe^{3+}-CS, 1.89 Å, is also within the covalent Fe−O bond length, as shown in Figure S4. Prior to binding, P(V) has a similar electronic structure as As(V) with high-energy O and Fe states near the Fermi level available for mixing and Fe^{3+}-P(V) complex formation (see Figure S4). Upon P(V) binding, there is a redistribution and overlap of the P(V) O states and Fe states to form a set of bonding and antibonding molecular orbitals and, thus, a covalent bond. The interactions stabilize electronic energies, causing a strong coordinate Fe−O bond between P(V) and Fe^{3+} (ICOHP = −4.7 eV/bond) consistent with the calculated bond length (1.89 Å). Like As(V), filled π^* antibonding states below the Fermi level are seen in the COHP plot (Figure 5b) for the Fe−O bond between P(V) and Fe^{3+} which again highlight that the bond is strengthened by Fe^{3+} back-donation (ICOHP for 3d-π^* orbital interaction = −0.7 eV/bond), partially filling the As−O π^* antibonding states.

Fe^{3+}-CS shows a slight energetic preference (0.1 eV) for As(V) over P(V), which we attribute to a difference in their π-acceptor strengths (back-donation extents) and molecular size that cause stronger Fe−O and H-bonds for As(V) than P(V). We quantify back-donation extents and thus π-acceptor strengths via the ICOHP values for the 3d−2p orbital interaction in the Fe−O bond of the Fe^{3+}−oxyanion complex, which has a more negative value (stronger) for As(V) (−0.8 eV/bond) than for P(V) (−0.7 eV/bond). In addition, the H-bond is slightly shorter and stronger (1.63 Å; ICOHP = −1.32 eV/bond) for As(V) than P(V) (1.67 Å; ICOHP = −0.57 eV/bond). Furthermore, Bader charge analysis reveals lower mean electron densities on the As(V) O atoms than on P(V) O atoms ($-0.27e^-$), suggesting that the less polarized oxyanion is a stronger π-acceptor in this metal−ligand interaction.

As(III) also binds more strongly to Fe^{3+}-CS, −1 eV, than neat CS but less strongly than the other two anions. As(III) binds in a monodentate configuration, unlike As(V) and P(V), and binding is less preferred by 0.9 and 0.8 eV, respectively. This weaker binding causes a longer Fe−O bond (2 Å) for As(III) (see Figure S4) than for As(V) and P(V), 1.89 and 1.89 Å, respectively. The Fe−O bond length for the Fe^{3+}-As(III) complex is 0.39 Å longer than the length reported for the second shell fit of the Fe^{3+}-As(III) complex (1.61 Å) obtained via EXAFS analysis.[39] The discrepancy in bond lengths may be due to the ∼0.2 Å variance in interatomic distances during EXAFS fitting noted by the authors. However, there is better agreement between our DFT calculations and EXAFS for the As−O bond of As(III) when bound to Fe^{3+}-CS, 1.92 and 1.79−1.8 Å,[39] respectively.

As(III) exhibits a distinct electronic structure from As(V) and P(V), both before and after binding to Fe^{3+}-CS. In contrast to the charged pair, the Fe^{3+}-CS-As(III) system is such that the near-Fermi region is populated mainly by Fe states with little contribution from the As(III)O states. Most As(III)O states are significantly lower in energy than the Fe states and thus are further removed from the Fermi level, as shown in Figure S4. The distribution of the As(III) O states indicates higher energetic stability and hence less reactivity of the O atoms than those of As(V) and P(V). The energetic mismatch between Fe^{3+} and As(III) states results in less mixing of the metal−ligand states during complex formation compared to As(V) and P(V), ultimately resulting in weaker binding. This is in agreement with the less negative ICOHP value (weaker bond) for the Fe−O bond for As(III), −3.5 eV/bond, than for As(V) and P(V), −4.9 and −4.7 eV/bond, respectively.

We attribute the differences in binding strength to the charge neutrality of As(III) compared to the negatively charged As(V) and P(V), which causes the latter to interact more favorably electrostatically and chemically with the positively charged Fe^{3+}. The stronger binding preference of P(V) over As(III) we have calculated (0.8 eV) is in contrast to the slightly preferential removal of As(III) in the presence of P(V) measured by Pincus et al.[39] The disagreement between our results and the experiment may be due to our consideration of the TMC binding sites in isolation, which does not account for possible electrostatic repulsions and thus weakened binding between adsorbed anionic species (As(V) and P(V)) at neighboring sites. Such repulsive forces would likely be significantly less for the charge-neutral As(III) and thus have less effect on its binding. Further, the large error reported in the experimental work could indicate large inhomogeneities associated with As(III) binding, which makes chemically accurate predictions difficult. Nonetheless, our model does indicate that Fe^{3+} significantly suppresses the preference for P(V), in this case by 0.2 eV, relative to neat CS.

https://doi.org/10.1021/acs.jpcb.3c06838
J. Phys. Chem. B 2024, 128, 1689−1699

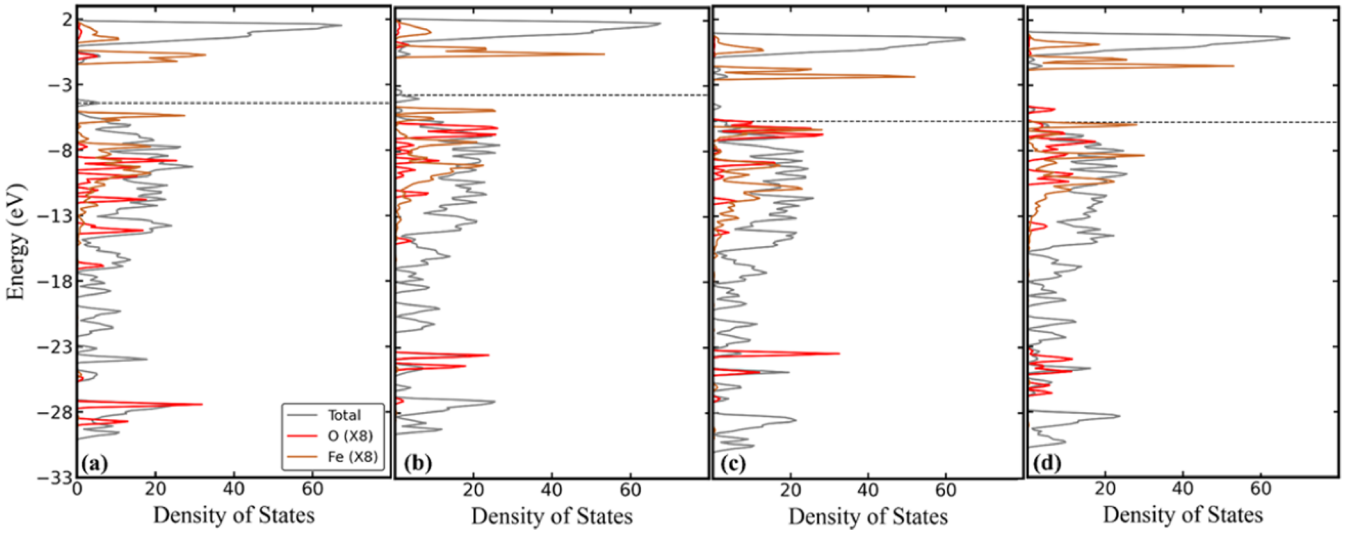

Figure 6. DOS plots for the different As(V) species in the Fe^{3+}-CS system. (a) H_3AsO_4, (b) $H_2AsO_4^-$, (c) $HAsO_4^{2-}$, and (d) AsO_4^{3-}.

Overall, the presence of P(V) is expected to impede As(III) adsorption on Fe^{3+}-CS more severely than As(V), in agreement with the previous findings of Pincus and co-workers.[39]

3.4. Effects of Protonation on Oxyanion Binding to Neat Chitosan. We examined the role of pH and oxyanion charge state on binding affinity and selectivity by calculating binding energies for As(V), As(III), and P(V) binding to neat CS as a function of oxyanion protonation extent, i.e., fully protonated (H_3XO_y), diprotonated ($H_2XO_y^-$), monoprotonated (HXO_y^{2-}), and deprotonated (XO_y^{3-}), where X represents As or P, while y represents the number of O atoms (4 for As(V) and P(V) and 3 for As(III)).

Oxyanion deprotonation destabilizes the electronic states of the oxidized species (increase in energy), as highlighted by the upward shifts of those states relative to the Fermi level with decreasing protonation extent. This is shown in the PDOS plots of Figure 6 for As(V). The closer the oxyanion electronic states are to the Fermi level, the more basic (reactive) the oxyanion.[74] As expected, we calculate that As(V) binds more strongly with decreasing protonation extent, 0.2, −0.2, −0.3, and −0.8 eV for H_3AsO_4, $H_2AsO_4^-$, $HAsO_4^{2-}$, and AsO_4^{3-}, respectively, as shown in Figure 7a, consistent with the decreased stability of the O states and increased electrostatic interactions with decreasing protonation extent. The fully protonated As(V), having the most stabilized O states, does not bind favorably with neat CS (0.2 eV), while the most destabilized deprotonated As(V) binds most strongly, −0.8 eV. The higher bond strengths with decreasing protonation extent cause shorter H-bonds, from 2.31 Å for the fully protonated state to 1.58 Å for the deprotonated state. The optimized structures for all As(V) species bound to neat CS are shown in Figure S5.

P(V) exhibits an identical monotonic trend in binding strength with protonation extent, 0.2, −0.2, −0.3, and −0.9 eV for H_3PO_4, $H_2PO_4^-$, HPO_4^{2-}, and PO_4^{3-}, respectively, as shown in Figure 7a. The optimized structures for all P(V) species bound to neat CS are shown in Figure S6. The chemical physics governing the P(V) trend is similar to that of As(V). Notably, neat CS has no preference for As(V) over P(V) at the various protonation states, and hence, we expect

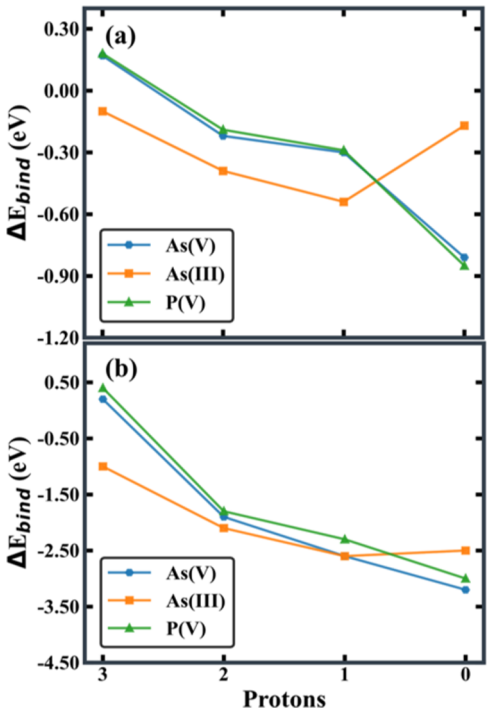

Figure 7. (a) Binding energies for As(V), As(III), and P(V) bound to neat CS at various protonation states. (b) Binding energies for As(V), As(III), and P(V) bound to Fe^{3+}-CS at various protonation states.

both species to be bound equally under all pH conditions and P(V) to inhibit As(V) removal.

Our calculations show that As(III) exhibits a nonmonotonic trend in binding strength with decreasing protonation extent on neat CS, −0.1, −0.4, −0.5, and −0.2 eV for H_3AsO_3, $H_2AsO_3^-$, $HAsO_3^{2-}$, and AsO_3^{3-}, respectively, shown in Figure 7a. Optimized structures for all As(III) species bound to neat CS are shown in Figure S7. As(III) is preferred over both As(V) and P(V) in all but the deprotonated state, where it is less preferred. We attribute this nonmonotonic behavior to the difference in the As(III) molecular structure between the deprotonated and other states. The deprotonated As(III) has larger O−As−O bond angles (105°) compared to those of the

https://doi.org/10.1021/acs.jpcb.3c06838
J. Phys. Chem. B 2024, 128, 1689−1699

other protonation states (100°), which strains the As(III) molecule and weakens its binding. This strained state is unlike As(V) and P(V), whose bond angles are preserved in all protonation states, and thus, their binding energy trends are monotonic.

Furthermore, the deprotonated As(III) binds in a monodentate configuration at an amine site, while both As(V) and P(V) bind bidentate to an amine and neighboring hydroxyl site and thus bind more strongly. We note that we tested multiple binding configurations, and these structures are the most stable ones. Despite the more favorable energetics we have calculated for As(III) compared to As(V) and P(V) at the fully, di-, and monoprotonated states, these preferences occur in protonation states that are very unlikely for As(III), given its pK_a of 9.2 relative to both As(V) and P(V), 6.9 and 7.2, respectively. Hence, we expect As(V) and P(V) to bind more favorably than As(III) to neat CS in environmental conditions where As(III) is fully protonated but As(V) and P(V) are semiprotonated.

3.5. Effects of Protonation on Oxyanion Binding to Fe^{3+}-Chitosan. Complementary calculations for binding the different oxyanion protonation states were performed for the Fe^{3+}-CS system. We calculate that binding strength increases monotonically with decreasing protonation extent for As(V) bound to Fe^{3+}-CS (Figure 7b). The fully protonated state binds endothermically by 0.2 eV, while the deprotonated state binds by −3.2 eV. This binding energy trend correlates with the mean Fe−O bond strengths of the different protonation states, which have ICOHP values of −2.6, −4.9, −11.4, and −12 eV/bond for the fully, di-, mono-, and deprotonated states, respectively. The increased Fe−O bond strengths with decreasing protonation extent caused shorter Fe−O bonds, from 2.18 Å for the fully protonated state to 1.84 Å for the deprotonated state. We also note differences in binding configurations where the fully protonated As(V) binds monodentate but the di-, mono-, and deprotonated states bind in bidentate configurations, resulting in stronger bonds for those states. Again, we attribute this trend in binding energy to the differences in electronic stability among the oxyanion protonation states. The closer the oxyanion electronic states are to the Fermi level, the more basic (reactive) the oxyanion,[74] causing the more favorable binding of the less protonated As(V) states.

P(V) behaves nearly identically to As(V). P(V) binding strength to Fe^{3+}-CS increases monotonically with decreasing protonation extent. P(V) binds by 0.4 eV in the fully protonated state, while it binds exothermically by −3 eV when deprotonated. Thus, As(V) is preferred over P(V) in all protonation states. We attribute the preference for As(V) over P(V) to the differences in their π-acceptor character, which cause As(V) to form more stabilized molecular orbitals in the Fe−O bonds with Fe^{3+}-CS than P(V), highlighted by the more negative 3d−2p orbital ICOHP values for As(V) than P(V), shown in Figure 8a. These binding energetics thus suggest that Fe^{3+}-CS would prefer As(V) over P(V) over a wide pH range across protonation states.

As(III) binding energies to Fe^{3+}-CS are nonmonotonic, being −1, −2.1, −2.6, and −2.5 eV for H_3AsO_3, $H_2AsO_3^-$, $HAsO_3^{2-}$, and AsO_3^{3-}, respectively. As(III) is preferred over both As(V) and P(V) in the fully and diprotonated states. Like neat CS, the nonmonotonic As(III) binding trend arises from its stretched O−As−O bond angles that induce strain and weaken binding in the mono- and deprotonated states. Just as in the case of neat CS, although As(III) has more favorable

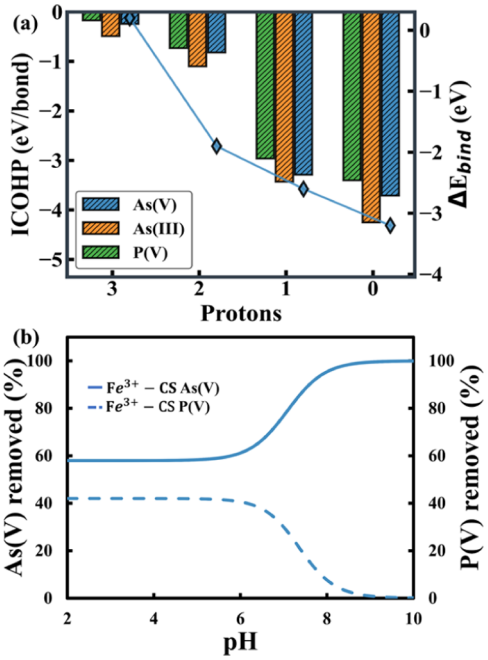

Figure 8. (a) ICOHP for 3d-π* interaction in the Fe−O bond for As(V), As(III), and P(V) bound to Fe^{3+}-CS at various protonation states; secondary *y*-axis shows As(V) binding energies at the various protonation states. (b) Predicted % As(V) and P(V) removed as a function of pH with 1:6 As(V)/P(V) ratio for Fe^{3+}-CS. Solid line is for As(V), while dashed line is for P(V).

binding energetics than As(V) and P(V) at the fully and diprotonated states, protonation state differences of the ions based on their pK_a means that the energetic effects at equivalent degrees of protonation are unrealistic. We, therefore, expect As(V) and P(V) to bind more favorably than As(III) to Fe^{3+}-CS at environmental conditions where As(III) is fully protonated and As(V) and P(V) are di- or monoprotonated.

Using our calculated binding energies, we predicted As(V) and P(V) uptake of Fe^{3+}-CS as a function of pH, assuming an excess of anions compared to the number of Fe^{3+} binding sites and a 1:6 molar ratio of As(V) to P(V) concentration, following the experimental work of Pincus et al.[39] As(III) was neglected because of the strong preference for As(V) and P(V) over As(III) under environmental conditions, as dictated by pK_a differences. The predicted removal of oxyanions is presented in Figure 8b, highlighting the As(V)/P(V) preference. This preference is delineated into three regimes: (1) pH < 6, where diprotonated states predominate; (2) pH between 6 and 8, characterized by varying protonation extents and equilibrium binding constants; and (3) pH > 8, where monoprotonated states dominate. In regime 1, the competition between As(V) and P(V) is quantified using eq 5, resulting in approximately 58% occupation of Fe^{3+} sites by As(V) due to its more favorable binding free energies (Figure S8). Regime 2 is complex due to multiple ion species and varying binding free energies with protonation extent, leading to steady As(V) uptake, achieving selective As(V) removal of ∼61% by Fe^{3+}-CS at pH 6. In regime 3 (pH > 8), where monoprotonated states prevail, As(V) dominates with over 95% occupation, consistent with experimental data showing ∼59% selective As(V) removal at pH 6 by Pincus et al.[39]

https://doi.org/10.1021/acs.jpcb.3c06838
J. Phys. Chem. B 2024, 128, 1689−1699

In summary, our findings indicate that selective separation of As(V) from P(V) is achievable with Fe^{3+}-CS under a wide range of pH conditions. However, the adsorption of As(III) is hindered by P(V) due to disparities in oxyanion pK_a and charge. Therefore, there is a need to explore modifications that enhance the preference for As(III) and increase the overall As removal capacity. Nevertheless, the predicted selectivity of As(V) over P(V) highlights the practical potential of Fe^{3+}-CS. Moreover, this selectivity is maintained even in excess of background P(V), underscoring the resilience and robustness of Fe^{3+}-CS as a promising sorbent for As removal applications.

4. CONCLUSIONS

In this work, we systematically utilized ab initio calculations to study the binding of As(V), P(V), and As(III) to neat chitosan and Fe^{3+}-chitosan. Our results show that at environmental conditions (with As(V) and P(V) in their deprotonated states and As(III) fully protonated), neat chitosan has no preference for arsenic over phosphate because the oxyanions bind to chitosan via weak H-bonds. Cross-linking chitosan with Fe^{3+} introduces high-energy 3d-states for chemical bonding with oxyanion 2p states of similar energy. Fe^{3+}-chitosan, therefore, binds the three oxyanions up to 10 times more strongly via coordinate covalent bonding using the 3d metal and 2p ligand electrons in the metal−ligand complex. We calculate that under environmental conditions, Fe^{3+}-chitosan favors As(V) over P(V) because of the more favorable Fe back-donation to As(V) than to P(V), which causes stronger Fe−O−As(V) bonds. This favorability arises because As(V) is a stronger π-acceptor than P(V). Conversely, both As(V) and P(V) are preferred over As(III) due to the charge neutrality of As(III) compared to the negatively charged As(V) and P(V), which causes the charged pair to form stronger Fe−O bonds with Fe^{3+}-chitosan.

We further elucidate a pH-dependent binding of arsenic by Fe^{3+}-chitosan and predict the selective removal of As(V) over P(V) from aqueous solutions in a wide pH range, which increases at elevated pH. While we calculated a binding energy preference for As(III) over both As(V) and P(V) in some protonation states, we note that it is of little consequence at environmental conditions due to differences in oxyanion pK_a's. These findings explain the improved performance of Fe^{3+}-chitosan for the selective removal of arsenic over phosphate and present an opportunity to leverage the new understanding for the rational design of selective organometallic sorbent materials by exploiting metal−ligand interactions. Specifically, different transition metal−ligand combinations and coordination environments yielding stronger π-donors should be explored to leverage the difference in π-accepting properties of arsenate and phosphate. This concept can also be extended to selectively removing other heavy-metal oxyanions with identical interfering ions from water.

■ ASSOCIATED CONTENT

Supporting Information

The Supporting Information is available free of charge at https://pubs.acs.org/doi/10.1021/acs.jpcb.3c06838.

Binding energies for As(V), As(III), and P(V) bound to Fc using different functionals; binding energies for As(V), As(III), and P(V) bound to Fc using different energy cut offs for the basis set; molecular model of neat chitosan; binding energies for the different oxyanion protonation extents on neat CS and Fe^{3+}-CS; optimized structures and DOS plots for P(V) and As(III) bound to neat CS; optimized structures and DOS plots for P(V) and As(III) bound to Fe^{3+}-CS; optimized structures for As(V) bound to neat CS and Fe^{3+}-CS for different protonation extents; optimized structures for P(V) bound to neat CS and Fe^{3+}-CS for different protonation extents; optimized structures for As(III) bound to neat CS and Fe^{3+}-CS for different protonation extents; binding free energies vs pH for Fe^{3+}-CS; predicted % As(V) and P(V) removed as a function of pH with different amounts of oxyanion solution-entropy loss; and thermodynamic data for oxyanions (PDF)

■ AUTHOR INFORMATION

Corresponding Author

Christopher Muhich − *Chemical Engineering, School for the Engineering of Matter, Transport and Energy, Arizona State University, Tempe, Arizona 85287, United States; Materials Science & Engineering, School for the Engineering of Matter, Transport and Energy, Arizona State University, Tempe, Arizona 85287, United States;* orcid.org/0000-0003-3089-559X; Phone: (480) 965-2673; Email: cmuhich@asu.edu

Author

Obinna Nwokonkwo − *Chemical Engineering, School for the Engineering of Matter, Transport and Energy, Arizona State University, Tempe, Arizona 85287, United States;* orcid.org/0009-0004-9862-3122

Complete contact information is available at: https://pubs.acs.org/10.1021/acs.jpcb.3c06838

Notes

The authors declare no competing financial interest.

■ ACKNOWLEDGMENTS

This work was supported by the National Institute of Environmental Health Sciences of the National Institutes of Health under Award Number P42ES030990 as part of the MEMCARE (Metals Mixtures: Cognitive Aging, Remediation, and Exposure Sources) project. This work was also partially supported by the Science and Technologies for Phosphorus Sustainability (STEPS) Center, a National Science Foundation Science and Technology Center (CBET-2019435). The content is solely the authors' responsibility and does not necessarily represent the official views of the National Institutes of Health or the National Science Foundation. In addition, the authors acknowledge support from Research Computing at Arizona State University for providing high-performance supercomputing services. The authors would also like to thank Dr. Julie Zimmermann, Dr. Lauren Pincus, and Dr. Holly Rudel for fruitful conversations.

■ REFERENCES

(1) Shaji, E.; Santosh, M.; Sarath, K. V.; Prakash, P.; Deepchand, V.; Divya, B. V. Arsenic contamination of groundwater: A global synopsis with focus on the Indian Peninsula. *Geosci. Front.* **2021**, *12* (3), No. 101079.

(2) Sun, G.; Yu, G.; Zhao, L.; Li, X.; Xu, Y.; Li, B.; Sun, D. Endemic Arsenic Poisoning. In *Endemic Disease in China*; Sun, D., Ed.; Springer Singapore, 2019; pp 97−123.

(3) Masindi, V.; Muedi, K. L.Environmental Contamination by Heavy Metals. In *Heavy metals*; IntechOpen, 2018; Vol. *10*, pp 115−132.
(4) Kumar, R.; Patel, M.; Singh, P.; Bundschuh, J.; Pittman, C. U., Jr.; Trakal, L.; Mohan, D. Emerging technologies for arsenic removal from drinking water in rural and peri-urban areas: Methods, experience from, and options for Latin America. *Sci. Total Environ.* **2019**, *694*, No. 133427.
(5) Fendorf, S.; Michael, H. A.; van Geen, A. Spatial and Temporal Variations of Groundwater Arsenic in South and Southeast Asia. *Science* **2010**, *328* (5982), 1123−1127.
(6) Terlecka, E. Arsenic Speciation Analysis in Water Samples: A Review of The Hyphenated Techniques. *Environ. Monit. Assess.* **2005**, *107* (1), 259−284.
(7) Xu, S.; Sabino, F. P.; Janotti, A.; Chase, D. B.; Sparks, D. L.; Rabolt, J. F. Unique Surface Enhanced Raman Scattering Substrate for the Study of Arsenic Speciation and Detection. *J. Phys. Chem. A* **2018**, *122* (49), 9474−9482.
(8) Smedley, P. L.; Kinniburgh, D. G. A review of the source, behaviour and distribution of arsenic in natural waters. *Appl. Geochem.* **2002**, *17* (5), 517−568.
(9) Sarkar, A.; Paul, B. The global menace of arsenic and its conventional remediation - A critical review. *Chemosphere* **2016**, *158*, 37−49.
(10) Sharma, Y. C.; Srivastava, V.; Singh, V. K.; Kaul, S. N.; Weng, C. H. Nano-adsorbents for the removal of metallic pollutants from water and wastewater. *Environ. Technol.* **2009**, *30* (6), 583−609.
(11) Banerji, T.; Kalawapudi, K.; Salana, S.; Vijay, R. Review of processes controlling arsenic retention and release in soils and sediments of Bengal basin and suitable iron based technologies for its removal. *Groundwater Sustainable Dev.* **2019**, *8*, 358−367.
(12) Jain, C. K.; Singh, R. D. Technological options for the removal of arsenic with special reference to South East Asia. *J. Environ. Manage.* **2012**, *107*, 1−18.
(13) Elimelech, M.; Phillip, W. A. The Future of Seawater Desalination: Energy, Technology, and the Environment. *Science* **2011**, *333* (6043), 712−717.
(14) Alka, S.; Shahir, S.; Ibrahim, N.; Ndejiko, M. J.; Vo, D.-V. N.; Manan, F. A. Arsenic removal technologies and future trends: A mini review. *J. Cleaner Prod.* **2021**, *278*, No. 123805.
(15) Mohan, D.; Pittman, C. U. Arsenic removal from water/wastewater using adsorbents—A critical review. *J. Hazard. Mater.* **2007**, *142* (1), 1−53.
(16) Lata, S.; Samadder, S. R. Removal of arsenic from water using nano adsorbents and challenges: A review. *J. Environ. Manage.* **2016**, *166*, 387−406.
(17) Strathmann, H. Electrodialysis, a mature technology with a multitude of new applications. *Desalination* **2010**, *264* (3), 268−288.
(18) Ahmaruzzaman, M.; Gupta, V. K. Rice Husk and Its Ash as Low-Cost Adsorbents in Water and Wastewater Treatment. *Ind. Eng. Chem. Res.* **2011**, *50* (24), 13589−13613.
(19) Lata, S.; Singh, P.; Samadder, S. Regeneration of adsorbents and recovery of heavy metals: a review. *Int. J. Environ. Sci. Technol.* **2015**, *12*, 1461−1478.
(20) Goldberg, S. Competitive Adsorption of Arsenate and Arsenite on Oxides and Clay Minerals. *Soil Sci. Soc. Am. J.* **2002**, *66* (2), 413−421.
(21) Jain, A.; Loeppert, R. H. Effect of Competing Anions on the Adsorption of Arsenate and Arsenite by Ferrihydrite. *J. Environ. Qual.* **2000**, *29* (5), 1422−1430.
(22) Pincus, L. N.; Rudel, H. E.; Petrovic, P. V.; Gupta, S.; Westerhoff, P.; Muhich, C. L.; Zimmerman, J. B. Exploring the Mechanisms of Selectivity for Environmentally Significant Oxo-Anion Removal during Water Treatment: A Review of Common Competing Oxo-Anions and Tools for Quantifying Selective Adsorption. *Environ. Sci. Technol.* **2020**, *54* (16), 9769−9790.
(23) Miller, S. M.; Spaulding, M. L.; Zimmerman, J. B. Optimization of capacity and kinetics for a novel bio-based arsenic sorbent, TiO2-impregnated chitosan bead. *Water Res.* **2011**, *45* (17), 5745−5754.
(24) Miller, S. M.; Zimmerman, J. B. Novel, bio-based, photoactive arsenic sorbent: TiO2-impregnated chitosan bead. *Water Res.* **2010**, *44* (19), 5722−5729.
(25) Pincus, L. N.; Lounsbury, A. W.; Zimmerman, J. B. Toward Realizing Multifunctionality: Photoactive and Selective Adsorbents for the Removal of Inorganics in Water Treatment. *Acc. Chem. Res.* **2019**, *52* (5), 1206−1214.
(26) Yamani, J. S.; Miller, S. M.; Spaulding, M. L.; Zimmerman, J. B. Enhanced arsenic removal using mixed metal oxide impregnated chitosan beads. *Water Res.* **2012**, *46* (14), 4427−4434.
(27) Shakoor, M. B.; Niazi, N. K.; Bibi, I.; Shahid, M.; Saqib, Z. A.; Nawaz, M. F.; Shaheen, S. M.; Wang, H.; Tsang, D. C. W.; Bundschuh, J.; et al. Exploring the arsenic removal potential of various biosorbents from water. *Environ. Int.* **2019**, *123*, 567−579.
(28) Agbovi, H. K.; Wilson, L. D. 1 - Adsorption processes in biopolymer systems: fundamentals to practical applications. In *Natural Polymers-Based Green Adsorbents for Water Treatment*; Kalia, S., Ed.; Elsevier, 2021; pp 1−51.
(29) Kwok, K. C. M.; Koong, L. F.; Chen, G.; McKay, G. Mechanism of arsenic removal using chitosan and nanochitosan. *J. Colloid Interface Sci.* **2014**, *416*, 1−10.
(30) Pontoni, L.; Fabbricino, M. Use of chitosan and chitosan-derivatives to remove arsenic from aqueous solutions—a mini review. *Carbohydr. Res.* **2012**, *356*, 86−92.
(31) Yamani, J. S.; Lounsbury, A. W.; Zimmerman, J. B. Towards a selective adsorbent for arsenate and selenite in the presence of phosphate: Assessment of adsorption efficiency, mechanism, and binary separation factors of the chitosan-copper complex. *Water Res.* **2016**, *88*, 889−896.
(32) Pincus, L. N.; Melnikov, F.; Yamani, J. S.; Zimmerman, J. B. Multifunctional photoactive and selective adsorbent for arsenite and arsenate: Evaluation of nano titanium dioxide-enabled chitosan cross-linked with copper. *J. Hazard Mater.* **2018**, *358*, 145−154.
(33) Youngran, J.; Fan, M.; Van Leeuwen, J.; Belczyk, J. F. Effect of competing solutes on arsenic(V) adsorption using iron and aluminum oxides. *J. Environ. Sci.* **2007**, *19* (8), 910−919.
(34) Manning, B. A.; Goldberg, S. Modeling Competitive Adsorption of Arsenate with Phosphate and Molybdate on Oxide Minerals. *Soil Sci. Soc. Am. J.* **1996**, *60* (1), 121−131.
(35) Costa, E. T. S.; Guilherme, L. R. G.; Lopes, G.; Lima, J. M.; Curi, N. Competitive Sorption of Arsenate and Phosphate on Aluminum Mining By-product. *Water, Air, Soil Pollut.* **2012**, *223* (8), 5433−5444.
(36) Chowdhury, S. R.; Yanful, E. K. Arsenic and chromium removal by mixed magnetite−maghemite nanoparticles and the effect of phosphate on removal. *J. Environ. Manage.* **2010**, *91* (11), 2238−2247.
(37) Hawthorne, F. C. A bond-topological approach to theoretical mineralogy: crystal structure, chemical composition and chemical reactions. *Phys. Chem. Miner.* **2012**, *39* (10), 841−874.
(38) Yazdani, M. R.; Bhatnagar, A.; Vahala, R. Synthesis, characterization and exploitation of nano-TiO 2 /feldspar-embedded chitosan beads towards UV-assisted adsorptive abatement of aqueous arsenic (As). *Chem. Eng. J.* **2017**, *316*, 370−382.
(39) Pincus, L. N.; Petrović, P. V.; Gonzalez, I. S.; Stavitski, E.; Fishman, Z. S.; Rudel, H. E.; Anastas, P. T.; Zimmerman, J. B. Selective adsorption of arsenic over phosphate by transition metal cross-linked chitosan. *Chem. Eng. J.* **2021**, *412*, No. 128582.
(40) Costa, M. P.; Prates, L. M.; Baptista, L.; Cruz, M. T.; Ferreira, I. L. Interaction of polyelectrolyte complex between sodium alginate and chitosan dimers with a single glyphosate molecule: A DFT and NBO study. *Carbohydr. Polym.* **2018**, *198*, 51−60.
(41) Singh, R.; Smiatek, J.; Moerschbacher, B. M. Unraveling the Impact of Acetylation Patterns in Chitosan Oligomers on Cu2+ Ion Binding: Insights from DFT Calculations. *Int. J. Mol. Sci.* **2023**, *24* (18), No. 13792.
(42) Rahangdale, D.; Archana, G.; Kumar, A. Molecularly imprinted chitosan-based adsorbents for the removal of salicylic acid and its molecular modeling to study the influence of intramolecular hydrogen

https://doi.org/10.1021/acs.jpcb.3c06838
J. Phys. Chem. B 2024, 128, 1689−1699

bonding of template on molecular recognition of molecularly imprinted polymer. *Adsorpt. Sci. Technol.* **2016**, *34* (7−8), 405−425.
(43) Jeremić, S.; Tran, T. H.; Marković, Z.; Ngo, T.; Dao, D. Q. Insight into interaction properties between mercury and lead cations with chitosan and chitin: Density functional theory studies. *Comput. Theor. Chem.* **2018**, *1138*, 99−106.
(44) Ezzat, H.; Menazea, A.; Omara, W.; Basyouni, O. H.; Helmy, S. A.; Mohamed, A. A.; Tawfik, W.; Ibrahim, M. DFT: B3LYP/LANL2DZ study for the removal of Fe, Ni, Cu, As, Cd and Pb with Chitosan. *Biointerface Res. Appl. Chem.* **2020**, *10*, 7002−7010.
(45) Wang, B.; Bai, Z.; Jiang, H.; Prinsen, P.; Luque, R.; Zhao, S.; Xuan, J. Selective heavy metal removal and water purification by microfluidically-generated chitosan microspheres: Characteristics, modeling and application. *J. Hazard. Mater.* **2019**, *364*, 192−205.
(46) Braier, N.; Jishi, R. Density functional studies of Cu2+ and Ni2+ binding to chitosan. *J. Mol. Struct.: THEOCHEM* **2000**, *499* (1−3), 51−55.
(47) Lü, R.; Cao, Z.; Shen, G. Comparative study on interaction between copper (II) and chitin/chitosan by density functional calculation. *J. Mol. Struct.: THEOCHEM* **2008**, *860* (1−3), 80−85.
(48) Terreux, R.; Domard, M.; Viton, C.; Domard, A. Interactions study between the copper II ion and constitutive elements of chitosan structure by DFT calculation. *Biomacromolecules* **2006**, *7* (1), 31−37.
(49) Portnyagin, A.; Bratskaya, S. Y.; Pestov, A.; Voit, A. Binding Ni (II) ions to chitosan and its N-heterocyclic derivatives: Density functional theory investigation. *Comput. Theor. Chem.* **2015**, *1069*, 4−10.
(50) Mishima, K.; Du, X.; Sekiguchi, S.; Kano, N. Experimental and theoretical studies on the adsorption and desorption mechanisms of chromate ions on cross-linked chitosan. *J. Funct. Biomater.* **2017**, *8* (4), No. 51.
(51) Wan, H.; Fang, F.; Shi, K.; Yi, Z.; Lei, L.; Li, S.; Mills, R.; Bhattacharyya, D.; Xu, Z. pH-Swing membrane adsorption of perfluoroalkyl substances: Anion-exchange brushes and role of water chemistry. *Sep. Purif. Technol.* **2024**, *329*, No. 124800.
(52) Kresse, G.; Furthmüller, J. Efficiency of ab-initio total energy calculations for metals and semiconductors using a plane-wave basis set. *Comput. Mater. Sci.* **1996**, *6* (1), 15−50.
(53) Kresse, G.; Furthmüller, J. Efficient iterative schemes for ab initio total-energy calculations using a plane-wave basis set. *Phys. Rev. B* **1996**, *54* (16), 11169−11186.
(54) Heyd, J.; Scuseria, G. E. Efficient hybrid density functional calculations in solids: Assessment of the Heyd−Scuseria−Ernzerhof screened Coulomb hybrid functional. *J. Chem. Phys.* **2004**, *121* (3), 1187−1192.
(55) Perdew, J. P.; Burke, K.; Ernzerhof, M. Generalized Gradient Approximation Made Simple. *Phys. Rev. Lett.* **1996**, *77* (18), 3865−3868.
(56) Kresse, G.; Joubert, D. From ultrasoft pseudopotentials to the projector augmented-wave method. *Phys. Rev. B* **1999**, *59* (3), 1758−1775.
(57) Grimme, S.; Antony, J.; Ehrlich, S.; Krieg, H. A consistent and accurate ab initio parametrization of density functional dispersion correction (DFT-D) for the 94 elements H-Pu. *J. Chem. Phys.* **2010**, *132* (15), No. 154104.
(58) Grimme, S.; Ehrlich, S.; Goerigk, L. Effect of the damping function in dispersion corrected density functional theory. *J. Comput. Chem.* **2011**, *32* (7), 1456−1465.
(59) Mathew, K.; Sundararaman, R.; Letchworth-Weaver, K.; Arias, T. A.; Hennig, R. G. Implicit solvation model for density-functional study of nanocrystal surfaces and reaction pathways. *J. Chem. Phys.* **2014**, *140* (8), No. 084106.
(60) Gupta, S.; Nguyen, N. A.; Muhich, C. L. Surface water H-bonding network is key controller of selenate adsorption on [012] α-alumina: An Ab-initio study. *J. Colloid Interface Sci.* **2022**, *617*, 136−146.
(61) Zhang, X.; Sewell, T. E.; Glatz, B.; Sarupria, S.; Getman, R. B. On the water structure at hydrophobic interfaces and the roles of water on transition-metal catalyzed reactions: A short review. *Catal. Today* **2017**, *285*, 57−64.
(62) Kwok, K. C. M.; Koong, L. F.; Al Ansari, T.; McKay, G. Adsorption/desorption of arsenite and arsenate on chitosan and nanochitosan. *Environ. Sci. Pollut Res.* **2018**, *25* (15), 14734−14742.
(63) Nelson, R.; Ertural, C.; George, J.; Deringer, V. L.; Hautier, G.; Dronskowski, R. LOBSTER: Local orbital projections, atomic charges, and chemical-bonding analysis from projector-augmented-wave-based density-functional theory. *J. Comput. Chem.* **2020**, *41* (21), 1931−1940.
(64) Ong, S. P.; Richards, W. D.; Jain, A.; Hautier, G.; Kocher, M.; Cholia, S.; Gunter, D.; Chevrier, V. L.; Persson, K. A.; Ceder, G. Python Materials Genomics (pymatgen): A robust, open-source python library for materials analysis. *Comput. Mater. Sci.* **2013**, *68*, 314−319.
(65) George, J.; Petretto, G.; Naik, A.; Esters, M.; Jackson, A. J.; Nelson, R.; Dronskowski, R.; Rignanese, G. M.; Hautier, G. Automated Bonding Analysis with Crystal Orbital Hamilton Populations. *ChemPlusChem* **2022**, *87* (11), No. e202200123.
(66) Lide (National Institute of Standards and Technology). *CRC Handbook of Chemistry and Physics*, 84th ed.; David, R., Ed.; CRC Press LLC: Boca Raton, 2004; Vol. *126*, pp 1586−1586 0−8493−0484−9.
(67) Zhu, X.; Nordstrom, D. K.; McCleskey, R. B.; Wang, R. Ionic molal conductivities, activity coefficients, and dissociation constants of HAsO42− and H2AsO4− from 5 to 90°C and ionic strengths from 0.001 up to 3molkg−1 and applications in natural systems. *Chem. Geol.* **2016**, *441*, 177−190.
(68) Nwokonkwo, O.; Pelletier, V.; Broud, M.; Muhich, C. Functionalized Ferrocene Enables Selective Electrosorption of Arsenic Oxyanions over Phosphate—A DFT Examination of the Effects of Substitutional Moieties, pH, and Oxidation State. *J. Phys. Chem. A* **2023**, *127* (37), 7727−7738.
(69) Hay, B. P.; Dixon, D. A.; Bryan, J. C.; Moyer, B. A. Crystallographic Evidence for Oxygen Acceptor Directionality in Oxyanion Hydrogen Bonds. *J. Am. Chem. Soc.* **2002**, *124* (2), 182−183.
(70) Jiang, C.; Zhang, T.; Li, S.; Yang, Z. A comparative study on Fe(III)-chitosan and Fe(III)-chitosan-CTAB composites for As(V) removal from water: preparation, characterization and reaction mechanism. *Environ. Sci. Pollut. Res.* **2022**, *29* (51), 77851−77863.
(71) Foppa, L.; Copéret, C.; Comas-Vives, A. Increased Back-Bonding Explains Step-Edge Reactivity and Particle Size Effect for CO Activation on Ru Nanoparticles. *J. Am. Chem. Soc.* **2016**, *138* (51), 16655−16668.
(72) Yan, L.; Hu, S.; Duan, J.; Jing, C. Insights from Arsenate Adsorption on Rutile (110): Grazing-Incidence X-ray Absorption Fine Structure Spectroscopy and DFT+U Study. *J. Phys. Chem. A* **2014**, *118* (26), 4759−4765.
(73) Yan, L.; Chan, T.; Jing, C. Arsenic adsorption on hematite facets: spectroscopy and DFT study. *Environ. Sci.: Nano* **2020**, *7* (12), 3927−3939.
(74) Moraes, P. I. R.; Tavares, S. R.; Vaiss, V. S.; Leitão, A. A. Ab Initio Study of Layered Double Hydroxides Containing Iron and Its Potential Use as Fertilizer. *J. Phys. Chem. C* **2016**, *120* (18), 9965−9974.

https://doi.org/10.1021/acs.jpcb.3c06838
J. Phys. Chem. B 2024, 128, 1689−1699